J|A|C|S ARTICLES

Published on Web 12/16/2009

# Binding of Coenzyme B Induces a Major Conformational Change in the Active Site of Methyl-Coenzyme M Reductase

Sieglinde Ebner,[†] Bernhard Jaun,*[,†] Meike Goenrich,[‡] Rudolf K. Thauer,[‡] and Jeffrey Harmer*[,§]

*Department of Chemistry, Centre for Advanced Electron Spin Resonance, University of Oxford, South Parks Road, Oxford OX1 3QR, United Kingdom, Laboratory of Organic Chemistry, ETH Zurich, 8093 Zurich, Switzerland, and Department of Biochemistry, Max Planck Institute for Terrestrial Microbiology, Karl-von-Frisch Strasse, 35043 Marburg, Germany*

Received July 29, 2009; E-mail: jeffrey.harmer@chem.ox.ac.uk; jaun@org.chem.ethz.ch

***Abstract:*** Methyl-coenzyme M reductase (MCR) is the key enzyme in methane formation by methanogenic Archaea. It converts the thioether methyl-coenzyme M and the thiol coenzyme B into methane and the heterodisulfide of coenzyme M and coenzyme B. The catalytic mechanism of MCR and the role of its prosthetic group, the nickel hydrocorphin coenzyme $F_{430}$, is still disputed, and no intermediates have been observed so far by fast spectroscopic techniques when the enzyme was incubated with the natural substrates. In the presence of the competitive inhibitor coenzyme M instead of methyl-coenzyme M, addition of coenzyme B to the active Ni(I) state $MCR_{red1}$ induces two new species called $MCR_{red2a}$ and $MCR_{red2r}$ which have been characterized by pulse EPR spectroscopy. Here we show that the two $MCR_{red2}$ signals can also be induced by the *S*-methyl- and the *S*-trifluoromethyl analogs of coenzyme B. $^{19}$F-ENDOR data for $MCR_{red2a}$ and $MCR_{red2r}$ induced by *S*-$CF_3$-coenzyme B show that, upon binding of the coenzyme B analog, the end of the 7-thioheptanoyl chain of coenzyme B moves closer to the nickel center of $F_{430}$ by more than 2 Å as compared to its position in both, the Ni(I) $MCR_{red1}$ form and the X-ray structure of the inactive Ni(II) $MCR_{ox1\text{-}silent}$ form. The finding that the protein is able to undergo a conformational change upon binding of the second substrate helps to explain the dramatic change in the coordination environment induced in the transition from $MCR_{red1}$ to $MCR_{red2}$ forms and opens the possibility that nickel coordination geometries other than square planar, tetragonal pyramidal, or elongated octahedral might occur in intermediates of the catalytic cycle.

## Introduction

Methyl-coenzyme M reductase (MCR) catalyzes the reduction of methyl-coenzyme M ($CH_3-S-CoM$, 2-(methylthio)ethane sulfonate) with coenzyme B (HS−CoB, 7-thioheptanoyl-threoninephosphate) to methane and CoM−S−S−CoB, which is the methane forming step in the energy metabolism of all methanogenic archaea.[1,2] MCR harbors the nickel porphyrinoid $F_{430}$, which is in the Ni(I) oxidation state when the enzyme is active.

$$CH_3-S-CoM + HS-CoB \rightarrow CH_4 + CoM-S-S-CoB \; \Delta G^{0'} = -30 \text{ kJ mol}^{-1} \quad (1)$$

Several crystal structures of MCR in an inactive state ($Ni^{II}$, $d^8$, $S = 1$) have been determined.[3−6] The enzyme has an interlinked $\alpha_2\beta_2\gamma_2$ subunit structure and contains two molecules of the nickel porphyrinoid cofactor $F_{430}$ (Scheme 1) that are approximately 50 Å apart. Coenzyme $F_{430}$, the prosthetic group of MCR,[7−10] is buried deep within the protein and is accessible from the exterior only via a 50 Å long channel, through which methyl-coenzyme M has to diffuse to reach $F_{430}$. The channel is designed such that the terminal SH-group of the heptanoyl arm of coenzyme B remains 8 Å from the nickel. $CH_3-S-CoM$ binding increases the affinity for HS−CoB binding (ordered Bi Bi mechanism), thus ensuring $CH_3-S-CoM$ enters the channel first. The available crystal structures differ in the species that are axially coordinated to the nickel center of $F_{430}$. All structures have the carboxamide oxygen of the α′-glutamine residue 147 (Scheme 1) coordinated axially from the distal face to the nickel ion. In $MCR_{silent}$, a sulfonate oxygen of CoM−S−S−CoB is

[†] ETH Zurich.
[‡] Max Planck Institute for Terrestrial Microbiology.
[§] University of Oxford.

(1) Thauer, R. K. *Microbiology* **1998**, *144* (9), 2377.
(2) Jaun, B.; Thauer, R. K. *Met. Ions Life Sci.* **2007**, *2*, 323.
(3) Ermler, U.; Grabarse, W.; Shima, S.; Goubeaud, M.; Thauer, R. K. *Science (Wash.)* **1997**, *278* (5342), 1457.
(4) Grabarse, W.; Mahlert, F.; Duin, E. C.; Goubeaud, M.; Shima, S.; Thauer, R. K.; Lamzin, V.; Ermler, U. *J. Mol. Biol.* **2001**, *309* (1), 315.
(5) Grabarse, W.; Mahlert, F.; Shima, S.; Thauer, R. K.; Ermler, U. *J. Mol. Biol.* **2000**, *303* (2), 329.
(6) Shima, S.; Goubeaud, M.; Vinzenz, D.; Thauer, R. K.; Ermler, U. *J. Biochem. (Tokyo)* **1997**, *121* (5), 829.
(7) Ellefson, W. L.; Whitman, W. B.; Wolfe, R. S. *Proc. Natl. Acad. Sci. U.S.A.* **1982**, *79* (12), 3707.
(8) Faerber, G.; Keller, W.; Kratky, C.; Jaun, B.; Pfalz, A.; Spinner, C.; Kobelt, A.; Eschenmoser, A. *Helv. Chim. Acta* **1991**, *74* (4), 697.
(9) Livingston, D. A.; Pfaltz, A.; Schreiber, J.; Eschenmoser, A.; Ankelfuchs, D.; Moll, J.; Jaenchen, R.; Thauer, R. K. *Helv. Chim. Acta* **1984**, *67* (1), 334.
(10) Pfaltz, A.; Jaun, B.; Faessler, A.; Eschenmoser, A.; Jaenchen, R.; Gilles, H. H.; Diekert, G.; Thauer, R. K. *Helv. Chim. Acta* **1982**, *65* (3), 828.

coordinated to the $Ni^{II}$ ion, whereas in $MCR_{ox1\text{-}silent}$ and $MCR_{red2\text{-}silent}$, the thiol(ate) sulfur of (H)S−CoM is coordinated from the proximal face. Attempts to obtain a crystal structure of active MCR have failed until now, probably due to the low redox potential of the Ni(II)/Ni(I) couple in $F_{430}$ which is below −600 mV and thus 200 mV below that of the hydrogen electrode at pH 7.

The catalytic mechanism of the reduction (eq 1) at the nickel center is disputed,[1,4,11,12] but all mechanistic proposals that appeared in the literature after the X-ray structures explicitly or tacitly assume that the terminal SH-group of the heptanoyl arm of coenzyme B remains 8 Å from the nickel as indicated by the crystal structure of the inactive enzyme containing $Ni^{II}F_{430}$ (Scheme 1). In essence there are two proposed mechanisms which mainly differ in the nature of the initial cleavage of the sulfur-carbon bond of $CH_3$−S−CoM. In mechanism "A", proposed by Pelmenschikov et al.[11,12] on the basis of density functional theory (DFT) calculations, the $Ni^{I}$ center is assumed to attack the thioether sulfur of $CH_3$−S−CoM, releasing as intermediates a methyl radical and the thiolate complex CoM−S−$Ni^{II}F_{430}$. Since HS−CoB is assumed fixed at 8 Å from $NiF_{430}$, the generated methyl radical from $CH_3$−S−CoM must move ca. 4 Å to abstract a hydrogen atom from HS−CoB, a controversial assumption. In mechanism "B", the $Ni^{I}$ center initially acts as a nucleophile attacking methyl-coenzyme M at the carbon of the $CH_3$−S group, generating a $CH_3$−$Ni^{III}F_{430}$ intermediate and HS−CoM.[2,4,13] A $CH_3$−$Ni^{III}F_{430}$ species has been shown to form when $CH_3Br$ (or $CH_3I$) is added to active MCR,[14−16] and a Ni-alkyl bond is formed when the irreversible inhibitor BPS ($BrCH_2CH_2CH_2SO_3^-$) reacts with the active enzyme.[17] Theoretical hybrid DFT calculations on a $CH_3$−$Ni^{III}F_{430}$ model complex indicate that it is stable and has the unusual ground-state configuration $(d_{xy})^2(d_{xz})^2(d_{yz})^2(d_{x^2-y^2})^1$.[14,18,19]

Active MCR exhibits an axial EPR spectrum characteristic of a d,[9] $S = {}^1/_2$, $Ni^{I}$ complex with the unpaired electron in the $3d_{x^2-y^2}$ orbital [20−26] and is designated $MCR_{red1}$. In the absence of substrates the species is designated $MCR_{red1a}$ ("a" for absence), in the presence of $CH_3$−S−CoM it is called $MCR_{red1m}$ ("m" for methyl coenzyme M), and in the presence of HS−CoM it is denoted $MCR_{red1c}$ ("c" for coenzyme M). By addition of the natural substrates $CH_3$−S−CoM and HS−CoB to active MCR (red1a) it has not been possible to trap or observe any intermediates of reaction eq 1. Substrate analogs are thus used to explore structural changes upon binding which are important in understanding the catalytic mechanism. One important set is $MCR_{red1a}$ + HS−CoM + HS−CoB, where the addition of HS−CoB to $MCR_{red1a}$ + HS−CoM induces the conversion of the $MCR_{red1c}$ signal into the $MCR_{red1cc}$ signal (which is very similar to $MCR_{red1c}$) and up to 50% into two EPR species called $MCR_{red2a}$ and $MCR_{red2r}$ after their axial and rhombic EPR spectra, respectively.[27,28] The $MCR_{red1}$ type signal generated from $MCR_{red1a}$ in the presence of HS−CoM and HS−CoB differs slightly from the species generated only in the presence of HS−CoM and is therefore in the following addressed to as $MCR_{red1cc}$ ("cc" for coenzyme M and coenzyme B). $MCR_{red2a}$ is assigned to a $Ni^{III}$ hydride complex, whereas $MCR_{red2r}$ has a Ni−S coordination from HS−CoM, rhombic principal *g*-values which are unusually high, and a very asymmetric spin density distribution on the four hydropyrrolic nitrogens of the macrocyle $F_{430}$.[27,29] This loss of near-equivalence of the four nitrogens in the tetrapyrrole macrocycle together with the pronounced rhombicity of the $MCR_{red2r}$ signal must be due to a strong electronic and/or geometric distortion of the coordination sphere of the nickel center. It has been proposed by us that binding of HS−CoB results in a conformational change of the protein that induces or is coupled to the geometric changes observed when

***Scheme 1.*** Coenzyme F430, the Prosthetic Group of Methyl-Coenzyme M Reductase[a]

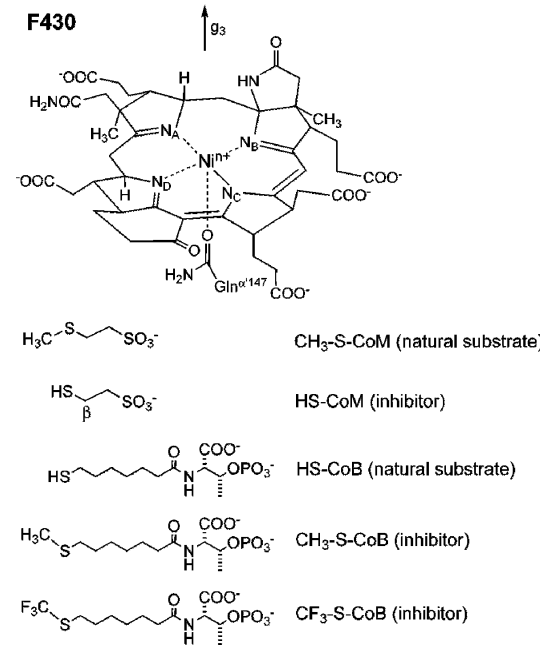


[a] The orientation of the axis $\mathbf{g}_3$ is shown. Shown are natural substrates $CH_3$−S−CoM and HS−CoB, and inhibitors HS−CoM ($\beta$ position indicated), $CH_3$−S−CoB, and $CF_3$−S−CoB.

(11) Pelmenschikov, V.; Blomberg, M. R. A.; Siegbahn, P. E. M.; Crabtree, R. H. *J. Am. Chem. Soc.* **2002**, *124* (15), 4039.
(12) Pelmenschikov, V.; Siegbahn, P. E. M. *J. Biol. Inorg. Chem.* **2003**, *8* (6), 653.
(13) Ermler, U. *J. Chem. Soc., Dalton* **2005**, (21), 3451.
(14) Yang, N.; Reiher, M.; Wang, M.; Harmer, J.; Duin, E. C. *J. Am. Chem. Soc.* **2007**, *129* (36), 11028.
(15) Dey, M.; Kunz, R. C.; Lyons, D. M.; Ragsdale, S. W. *Biochemistry* **2007**, *46* (42), 11969.
(16) Dey, M.; Telser, J.; Kunz, R. C.; Lees, N. S.; Ragsdale, S. W.; Hoffman, B. M. *J. Am. Chem. Soc.* **2007**, *129* (36), 11030.
(17) Hinderberger, D.; Piskorski, R. P.; Goenrich, M.; Thauer, R. K.; Schweiger, A.; Harmer, J.; Jaun, B. *Angew. Chem., Int. Ed.* **2006**, *45* (22), 3602.
(18) Wondimagegn, T.; Ghosh, A. *J. Am. Chem. Soc.* **2001**, *123* (7), 1543.
(19) Sarangi, R.; Dey, M.; Ragsdale, S. W. *Biochemistry* **2009**, *48* (14), 3146.
(20) Goubeaud, M.; Schreiner, G.; Thauer, R. K. *Eur. J. Biochem.* **1997**, *243* (1/2), 110.
(21) Jaun, B.; Pfaltz, A. *J. Chem. Soc., Chem. Commun.* **1986**, (17), 1327.
(22) Mahlert, F.; Bauer, C.; Jaun, B.; Thauer, R. K.; Duin, E. C. *J. Biol. Inorg. Chem.* **2002**, *7* (4−5), 500.
(23) Mahlert, F.; Grabarse, W.; Kahnt, J.; Thauer, R. K.; Duin, E. C. *J. Biol. Inorg. Chem.* **2002**, *7* (1−2), 101.
(24) Rospert, S.; Boecher, R.; Albracht, S. P. J.; Thauer, R. K. *FEBS Lett.* **1991**, *291* (2), 371.
(25) Rospert, S.; Voges, M.; Berkessel, A.; Albracht, S. P. J.; Thauer, R. K. *Eur. J. Biochem.* **1992**, *210* (1), 101.
(26) Telser, J.; Fann, Y. C.; Renner, M. W.; Fajer, J.; Wang, S. K.; Zhang, H.; Scott, R. A.; Hoffman, B. M. *J. Am. Chem. Soc.* **1997**, *119* (4), 733.
(27) Harmer, J.; Finazzo, C.; Piskorski, R.; Ebner, S.; Duin, E. C.; Goenrich, M.; Thauer, R. K.; Reiher, M.; Schweiger, A.; Hinderberger, D.; Jaun, B. *J. Am. Chem. Soc.* **2008**, *130* (33), 10907.
(28) Kern, D. I.; Goenrich, M.; Jaun, B.; Thauer, R. K.; Harmer, J.; Hinderberger, D. *J. Biol. Inorg. Chem.* **2007**, *12* (8), 1097.
(29) Finazzo, C.; Harmer, J.; Jaun, B.; Duin, E. C.; Mahlert, F.; Thauer, R. K.; Van Doorslaer, S.; Schweiger, A. *J. Biol. Inorg. Chem.* **2003**, *8* (5), 586.

going from the axial $MCR_{red1/2a}$ species to $MCR_{red2r}$.[27] Our principal aim in this work is to determine what structural changes occur when HS−CoB binds to active MCR.

Interestingly, the $MCR_{red2}$ signals can also be induced when the terminal SH group of CoB is replaced by a methylthioether group ($CH_3$−S−CoB).[27] In fact, this combination of substrate analogs has a very similar overall size as the natural substrates $CH_3$−S−CoM + HS−CoB (the methyl group of $CH_3$−S−CoM and thiol group of HS−CoB have been swapped). This observation prompted us to speculate that a $CF_3$−S- group, despite being somewhat larger than $CH_3$−S, might still be able to induce $MCR_{red2}$. Such a fluorine label at the end of the heptanoyl tail of coenzyme B would allow geometric changes to be monitored through measurement of the $^{19}F$ ($I = 1/2$) hyperfine interactions to determine the position of the $CF_3$ group of bound $CF_3$−S−CoB relative to the nickel. If the conformation in the active $Ni^{I}$ states is similar to that found in the X-ray structure of inactive $Ni^{II}F_{430}$, then the distance between the three F atoms and the nickel ion will be 6.2−7.7 Å. In this paper we first show that, like HS−CoB or $CH_3$−S−CoB, $CF_3$−S−CoB induces the two red2 species, and then determine the positions of CoB relative to $NiF_{430}$, for red1cc/red2a/red2r, using measured $^{19}F$ hyperfine couplings.

## Materials and Methods

**General.** THF was destilled over K under nitrogen, DMF was freshly destilled under vacuum at ca. 10 mbar and 40 °C over a fractionating column (110 cm) packed with glass beads. The reflux ratio was 10:1, and the middle fraction (30%) of the destillate was used. Amberlite IR-120 ($H^+$ form, 16−45 mesh) was conditioned by washing with ethanol until the eluent was colorless, stirring in 20% $H_2SO_4$ for 1 h, and washed with water until the eluent was neutral. XAD-2-polystyrene was purchased from Serva Electrophoresis, Germany. All other routine chemicals were obtained from Fluka, Aldrich, J.T. Baker and Merck and were used without further purification. Acid−base extraction was performed with concentrated HCl(aq) and saturated aqueous bicarbonate solution. RP-HPLC was performed with an Atlantis $dC_{18}$ 5 $\mu$m column, 19 mm × 50 mm with the following gradient program: $H_2O$/acetonitrile (4:1) → 100% acetonitrile in 70 min. Detection was performed on Alugram SIL G/$UV_{254}$ TLC plates (silica gel 60 with fluorescent indicator $UV_{254}$) in *n*-butanol/$H_2O$/acetic acid, 2:1:1 (v/v), staining with Mostain-solution (20 g $(NH_4)_6Mo_7O_{24}\cdot 4H_2O$ in 10% $H_2SO_4$, v/v (400 mL) and 0.4 g $CeSO_4$ in $H_2SO_4$ conc. (4 mL)). For desalting of **5** an Oasis HLB 35 $cm^3$ cartridge was conditioned first with MeOH, second with 1 N HCl. Then, the product was applied, desalted with 5 loads of water, and eluted with 100% MeOH. For the synthesis of coenzyme B derivatives, appropriately modified procedures of Ellerman et al.[30] were followed.

**Synthesis of (+)-(2*S*,3*R*)-*N*-[7-(Methylthio)heptanoyl]-*O*-phospho-L-threonine (1) [$CH_3$−S−CoB ($NH_4^+$ Form)]. 7-Bromoheptanoic Acid (2).[31]** Ethyl 7-bromo heptanoate (4.1 mL, 21.04 mmol) and aqueous hydrobromic acid (48%; 14.4 mL) were stirred at 130 °C (oil bath temperature) for 5 h. The cooled reaction mixture was diluted with water, extracted with dichloromethane and dried. Then acid−base extraction was perfomed to give 3.80 g (86%) of a white solid. $^1H$ NMR ($CDCl_3$, 300 MHz) $\delta$ 1.37−1.47 (m, 4H), 1.63−1.68 (m, 2H), 1.84−1.89 (m, 2H), 2.37 (t, 2H). $^{13}C$ NMR ($CDCl_3$, 300 MHz) $\delta$ 24.53, 27.88, 28.57, 32.60, 33.86, 34.00, 179.81.

**7-(Methylthio)heptanoic Acid[30] (3). 2** (0.9 g, 4.30 mmol) was dissolved in 12 mL of ethanol under nitrogen. First, 0.43 mL of a 10 M sodium hydroxide solution, then 0.313 g of sodium methanethiolate (4.47 mmol) were added slowly at 0 °C. The suspension was stirred for 2 h at 0 °C and 1 h at room temperature. After adding 2 mL of water, the reaction mixture was stirred at room temperature for 24 h, then poured on 25 mL of a 10% aqueous hydrochloride solution, extracted with diethylether, and dried to give 0.748 g (98%) of a yellow oil. $^1H$ NMR ($CDCl_3$; 300 MHz) $\delta$ 1.38 (m, 4H), 1.61 (m, 4H), 2.08 (s, 3H), 2.34 (t, 2H), 2,47 (t, 2H) ppm.

**7-(Methylthio)heptanoyl-*N*-hydroxysuccinimide Ester[30] (4). 3** (0.735 g, 4.2 mmol) and 0.503 g of *N*-hydroxysuccinimide (4.4 mmol) were dissolved in 25 mL anhydrous dioxane under nitrogen. After addition of 858 mg of dicyclohexylcarbodiimide (4.2 mmol), the reaction mixture was stirred for 16 h at room temperature. The precipitated dicyclohexylurea was removed by filtration and washed with dioxane (3 × 10 mL) followed by isopropanol (2 × 10 mL). The combined filtrates were dried to give a yellow oil which was purified by flash column chromatography ($rf = 0.2$; silica gel; dietlyl ether/ hexane, 2:1, v/v). The combined fractions containing pure **4** were dried to give 0.667 g (62%) of a viscous yellowish oil which solidified at −18 °C. $^1H$ NMR ($CDCl_3$; 200 MHz) $\delta$ 1.35−1.43 (m, 4H), 1.54−1.60 (m, 2H), 1.68−1.72 (m, 2H), 2.05 (s, 3H), 2.45 (t, 2H), 2.57 (t, 2H), 2.80 (s, 4H). $^{13}C$ NMR ($CDCl_3$; 200 MHz) $\delta$ 15.4, 24.3, 25.5 (2C), 28.1, 28.2, 28.7, 30.7, 33.9, 168.6, 169.2 (2C).

**(+)-(2*S*,3*R*)-*N*-[7-(Methylthio)heptanoyl]-*O*-phospho-L-threonine[30] (1) [$CH_3$S−CoB ($NH_4^+$ Form)].** A solution of 495 mg of *O*-phospho-L-threonine (2.48 mmol) and 849 $\mu$L of diisopropylethylamine (4.96 mmol) in 5 mL water was added to a solution of **4** (612 mg; 2.23 mmol) in 40 mL THF. Addition of acetonitrile (14 mL) resulted in a homogeneous colorless reaction mixture which was stirred at room temperature under nitrogen for 18 h. The dried residue was purified by RP-HPLC, then desalted and further purified by applying to an XAD-2-polystyrene column, dried, dissolved in approximately 2 mL of water, treated with concentrated $NH_3$(aq) to pH 7−8 and lyophylized to give 198 mg of pure **1** (ammonium salt; 0.53 mmol; 23%). $^1H$ NMR ($CD_3OD$; 400 MHz) $\delta$ 1.31 (d, $J = 2.89$, 2H), 1.35−1.45 (m, 4H), 1,56−1.66 (m, 4H), 2.06 (s, 3H), 2.29−2.33 (m, 2H), 2.48 (t, $J = 7.29$, 2H), 4.30 (d, $J = 2.65$, 1H), 4.72 (m, 1H). $^{13}C$ NMR ($CD_3OD$; 400 MHz) $\delta$ 15.4, 19.6, 26.9, 30.1, 35.0, 37.1, 61.1, 73.8, 172.2, 176.0. $^{31}P$ NMR ($CD_3OD$; 300 MHz): $\delta$ 1.32 (d, $J = 8.77$). ESI-MS: *m/z* 388.1 (6), 139.1 (6), 193.8 (6), 95.2 (9), 357.1 (15), 177.6 (51), 356.1 (100).

**Synthesis of (+)-(2*S*,3*R*)-*N*-[7-(Trifluoromethylthio)heptanoyl]-*O*-phospho-L-threonine (5) [$CF_3$S−CoB ($NH_4^+$ Form)]. 7-Mercaptoheptanoic Acid (6).** According to a modified procedure of Noll et al.,[32] a solution of 3.5 g of **2** (16.7 mmol) and 6.37 g of thiourea (83.7 mmol) in 100 mL acetone was refluxed under nitrogen at 70 °C for 17 h. The cooled (room temperature) and dried residue was added to a degassed (Ar) solution of 6.56 g of KOH (116.9 mmol) in 140 mL of ethanol, refluxed for another 4 h at 90 °C under nitrogen, and cooled to room temperature. Acid−base extraction was performed to give 2.61 g of pure **6** (16.08 mmol; 96%). $^1H$ NMR ($CDCl_3$; 200 MHz) $\delta$ 1.29−1.43 (m, 4H), 1.59−1.69 (m, 4H), 2.36 (t, 2H), 2.47−2.58 (q, 2H). $^{13}C$ NMR ($CDCl_3$; 200 MHz) $\delta$ 24.5, 27.9, 28.4, 33.7, 33.8, 180.0.

**7-(Trifluoromethylthio)heptanoic Acid (7).** According to a procedure of Soloshonok et al. [33] for the synthesis of *S*-trifluoromethyl-containing amino acids, **7** was synthesized by gradually introducing 90 mL of liquid ammonia (1.6 equiv) to 2 g of **6** (12.33 mmol) at −45 °C, and adding approximately 2 mL of trifluoromethyliodide (1.6 equiv, by cold pipetting). The reaction mixture was kept (stirring was not possible, since **7** solidified in the flask and the stirrer could not be moved) under UV irradiation (Hg lamp) for 4 h at −45 °C. The negative result of the Ellmann-Test[34] showed

(30) Ellermann, J.; Kobelt, A.; Pfaltz, A.; Thauer, R. K. *FEBS Lett.* **1987**, *220* (2), 358.
(31) Rao, A. V. R.; Reddy, S. P. *Synth. Commun.* **1986**, *16* (10), 1149.
(32) Noll, K. M.; Donnelly, M. I.; Wolfe, R. S. *J. Biol. Chem.* **1987**, *262* (2), 513.
(33) Soloshonok, V.; Kukhar, V.; Pustovit, Y.; Nazaretian, V. *Synlett* **1992**, (8), 657.
(34) Ellman, G. L. *Arch. Biochem. Biophys.* **1959**, *82* (1), 70.

that the thiol had been fully converted. After evaporation of the excess of ammonia, the residue was dissolved in 5 mL of water, acidified with 2 M HCl, extracted with diethyl ether, and dried. Flash column chromatography (silica gel; dichloromethane/ ethyl acetate/ acetic acid, 98:10:2, v/v) gave 2.30 g of pure **7** (9.97 mmol; 81%). $^1$H NMR ($CDCl_3$; 300 MHz) $\delta$ 1.36−1.44 (m, 4H), 1.61−1.73 (m, 4H), 2.36 (t, 2H), 2.87 (t, 2H), 8.5 (s, *b*). $^{13}$C NMR ($CDCl_3$; 300 MHz, $\tau$ = 4 s) $\delta$ 24.3, 28.0, 28.3, 29.2, 29.6−29.8 (q, $J$ = 2.3), 33.8, 134.2 (q, $J$ = 305.7), 179.7.

**7-(Trifluoromethylthio)heptanoyl-*N*-hydroxysuccinimide Ester[30] (8).** According to the synthesis of the analog ester **4**, 744 mg of **7** (3.23 mmol) and 409 mg of *N*-hydroxysuccinimide (3.55 mmol) were dissolved in 20 mL anhydrous dioxane under nitrogen. After addition of 667 mg of dicyclohexylcarbodiimide (3.23 mmol), the reaction mixture was stirred for 24 h at room temperature. The precipitated dicyclohexylurea was removed by filtration and washed with dioxane (3 × 10 mL) followed by isopropanol (2 × 10 mL). The combined filtrates were dried and 136 mg of the crude product was purified by flash column chromatography (silica gel; dietlyl ether/ hexane, 2:1, v/v). The combined fractions containing pure **8** were dried to give 640 mg of **8** (1.95 mmol; 61%). $^1$H NMR ($CDCl_3$; 300 MHz) $\delta$ 1.45 (m, 4H), 1.74 (m, 4H), 2.61 (t, 2H), 2.84 (s, 4H), 2.88 (t, 2H).

**(+)-(2*S*,3*R*)-*N*-[7-(Trifluoromethylthio)heptanoyl]-*O*-phospho-L-threonine[30] (5) [$CF_3S$−CoB ($NH_4^+$ Form)].** A solution of 427 mg *O*-phospho-L-threonine (2.15 mmol) and 668 $\mu$L diisopropylethylamine (3.90 mmol) in 5 mL water was added to a solution of **8** (640 mg; 1.95 mmol) in 20 mL THF. Addition of acetonitrile (10 mL) resulted in a homogeneous colorless reaction mixture which was stirred at room temperature under nitrogen for 36 h. The dried residue was purified by applying to an XAD-2-polystyrene column, dried, and desalted on an Oasis HLB 35 cm$^3$ cartridge, dissolved in 2 mL of water, treated with concentrated $NH_3$(aq) to pH 7−8 and lyophylized to give 98 mg of pure **5** (ammonium salt; 0.20 mmol; 10%). $^1$H NMR ($CD_3OD$; 400 MHz) $\delta$ 1.32 (d, $J$ = 6.34, 3H), 1.37−1.48 (m, 4H), 1.62−1.73 (m, 4H), 2.32 (t, $J$ = 7.51, 2H), 2.94 (t, $J$ = 7.39, 2H), 4.31 (d, $J$ = 3.54, 1H), 4.70−4.72 (m, 1H). $^{13}$C NMR ($CD_3OD$; 400 MHz) $\delta$ 19.6, 26.7, 29.2, 29.7, 30.6, 30.8, 36.9, 60.5, 73.2, 128.4−137.5 (q, $J$ = 304.4), 175.7, 176.2. $^{31}$P NMR ($CD_3OD$; 300 MHz): $\delta$ 0.87 (d, *b*, $J$ = 8.71). $^{19}$F NMR ($CD_3OD$; 300 MHz): $\delta$ −61.7 (s). ESI-MS: *m/z* 410 (100), 312 (27), 205 (23), 411 (15), 330 (14), 216 (11).

**Protein Purification and Sample Preparation.** *Methanothermobacter marburgensis* is the strain deposited under DSM 2133 in the Deutsche Sammlung von Mikroorganismen and Zellkulturen (Braunschweig). Methyl-coenzyme M reductase isoenzyme I from *Methanothermobacter marburgensis* was purified as previously described.[23] All the buffers used during purification contain 10 mM HS−CoM. Therefore the obtained enzyme was in the $MCR_{red1c}$ form. The spin concentration per mole of $F_{430}$ was approximately 0.8−0.9. The protein concentration was determined by measuring the absorbance difference of oxidized enzyme ($MCR_{silent}$) at 420 nm using $\varepsilon$ = 44 000 M$^{-1}$ cm$^{-1}$ for a molecular mass of 280 000 Da. For sample preparation the enzyme was concentrated extensively using an Amicon centrifugation cell with a 100 kDa cutoff (Millipore, Bedford MA). The two red2 species were induced by addition of $CF_3$−S−CoB to a concentration of 20 mM. EPR samples were frozen in liquid nitrogen for shipping and storage.

**EPR Spectroscopy (Sample Control).** As a control of the sample quality and concentration, 1−10 diluted samples (0.35 mL) were analyzed for EPR spectra at 77 K in 0.3 cm (inner diameter) quartz tubes with 95% $N_2$/5% $H_2$ as gas phase and closed with a closed-off rubber tube. The samples contained approximately 9.6 mg MCR (35 nmol) in 10 Tris/HCl pH 7.6. CW EPR spectra at X-band were recorded with a Bruker EMX-6/1 EPR spectrometer composed of an EMX 1/3 console, an ER 041 X6 bridge with built-in ER-0410−116 microwave (mw) frequency counter, an ER-070 magnet and an ER-4102st standard universal rectangular cavity. Spin quantifications were carried out under nonsaturating conditions using 10 mM copper perchlorate as a standard (10 mM $CuSO_4$; 2 M $NaClO_4$; 10 mM HCl). All signal intensities are expressed as spins per mol $F_{430}$. These EPR data were used exclusively for sample quality control, all experimental spectra shown in this paper are described below.

**EPR Spectroscopy.** Measurements at X- and W-band were carried out on a Bruker Elex 680 spectrometer, and at Q-band (35.3 GHz) on a home-built instrument,[35] both of which were equipped with a Helium gas-flow cryostat from Oxford Inc. The field-swept frozen-solution (15 K) W-band EPR spectra were recorded by integrating over the echo created with the mw pulse sequence $\pi/2-\tau-\pi-\tau-echo$, with mw pulse lengths $t_{\pi/2}$ = 100 ns, $t_\pi$ = 200 ns, and an interpulse delay of $\tau$ = 700 ns. The first derivative of this spectrum was calculated numerically. The field was calibrated using the two central lines from a CaO sample containing manganese ions. The $^{19}$F Mims-ENDOR spectra were measured at 15 K with the mw pulse sequence $\pi/2-\tau-\pi/2-T-\pi/2-\tau-echo$, with mw pulses of length $t_{\pi/2}$ = 32 ns, $\tau$ = 200−500 ns, and a shot repetition time of 5 ms. A radio frequency pulse of length 23 $\mu$s and variable frequency $\nu_{ENDOR}$ was applied during time $T$. The Q-band $^1$H Davies-ENDOR spectra were measured at 20 K with the mw pulse sequence $\pi-T-\pi/2-\tau-\pi-\tau-echo$, with mw pulses of length $t_{\pi/2}$ = 28 ns and $t_\pi$ = 56 ns, and $\tau$ = 160 ns. A radio frequency pulse of length 8.5 $\mu$s and variable frequency $\nu_{ENDOR}$ was applied during time $T$. X-band HYSCORE experiments at 25 K employed the pulse sequence $\pi/2-\tau-\pi/2-t_1-\pi-t_2-\pi/2-\tau-echo$ with mw pulses of lengths $t_{\pi/2}$ = $t_\pi$ = 16 ns, $\tau$ = 120 ns, and starting times $t_{1,0}$ = $t_{2,0}$ = 96 ns with increments $\Delta t$ = 16 ns (data matrix 300 × 300). An eight-step phase cycle was used to remove unwanted echoes. The HYSCORE data were processed with MATLAB 7.0 (The MathWorks, Inc.). The time traces were baseline corrected with an exponential, apodized with a Gaussian window and zero filled. After a two-dimensional Fourier transformation absolute-value spectra were calculated. Spectra recorded with different $\tau$ values were added to eliminate $\tau$-dependent blind spots. The EPR and Davies-ENDOR spectra were simulated with the program EasySpin.[36] HYSCORE spectra were simulated with a program written in-house.[37]

## Results

First EPR data are presented which show that the sample preparation [$CF_3$−S−CoB]-MCR, like [HS−CoB]-MCR, produces the three components red1c/red2a/red2r. Figure 1 presents W-band echo-detected EPR spectra for the complexes (A) $MCR_{red1c}$ (red1a + HS−CoM), (B) $MCR_{red1c}$ + HS−CoB, and (C) $MCR_{red1c}$ + $CF_3$−S−CoB. To simulate the $MCR_{red1c}$ spectrum, a two component model was required as can be appreciated by inspection of the $g_3$ feature at the low field end of the spectrum where there are two partially resolved peaks. The three features marked with a "*" belong to the species $MCR_{ox1}$.[38] Addition of either HS−CoB (Figure 1B) or $CF_3$−S−CoB (Figure 1C) to $MCR_{red1c}$ results in a dramatic spectral change that in both cases can be simulated by three components, a $MCR_{red1cc}$, virtually unchanged from $MCR_{red1c}$, and two $MCR_{red2}$ species labeled $MCR_{red2r}$ (rhombic spectrum) and $MCR_{red2a}$ (axial spectrum).[27,28] The $g$-values and relative intensities of the three species are given in Table 1 (the related preparation with $CH_3$−S−CoB is included for reference). Clearly the induction of the two $MCR_{red2}$ species

(35) Gromov, I.; Shane, J.; Forrer, J.; Rakhmatoullin, R.; Rozentzwaig, Y.; Schweiger, A. *J. Magn. Reson.* **2001**, *149* (2), 196.
(36) Stoll, S.; Schweiger, A. *J. Magn. Reson.* **2006**, *178* (1), 42.
(37) Madi, Z. L.; Van Doorslaer, S.; Schweiger, A. *J. Magn. Reson.* **2002**, *154* (2), 181.
(38) Harmer, J.; Finazzo, C.; Piskorski, R.; Bauer, C.; Jaun, B.; Duin, E. C.; Goenrich, M.; Thauer, R. K.; Van Doorslaer, S.; Schweiger, A. *J. Am. Chem. Soc.* **2005**, *127* (50), 17744.

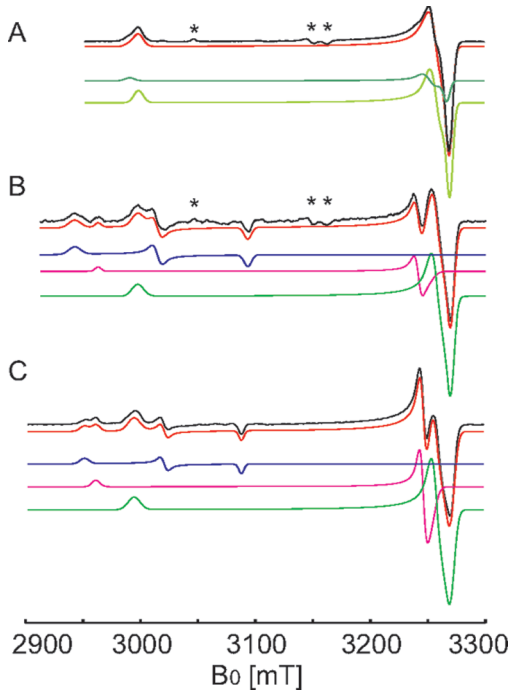


***Figure 1.*** W-band (94.2556 GHz) echo-detected EPR spectra (numerical 1st derivative) measured at 15 K of (A) $MCR_{red1a}$ + HS−CoM ($MCR_{red1c}$), (B) $MCR_{red1a}$ + HS−CoM + HS−CoB, and (C) $MCR_{red1a}$ + HS−CoM + $CF_3$−S−CoB. Experimental, black. Simulations: red, sum; (A) dark green, red1c (1st); light green, red1c (2nd); (B/C) blue, red2r; magenta, red2a; green, red1cc. "*" indicates $MCR_{ox1}$ features.

***Table 1.*** Amplitudes (*A*%) and *g*-Values for the Three States in $MCR_{red1/red2}$ Samples Prepared with HS−CoB, $CH_3$−S−CoB, and $CF_3$−S−CoB

| preparation | state | *A*% | $g_1, g_2, g_3$[a] |
|---|---|---|---|
| $MCR_{red1a}$ + HS−CoM + HS−CoB | red1cc | 69 | 2.0598, 2.0671, 2.2467 |
| | red2a | 14 | 2.0731, 2.0771, 2.2727 |
| | red2r | 17 | 2.2885, 2.2339, 2.1771 |
| $MCR_{red1a}$ + HS−CoM + $CH_3$−S−CoB | red1cc | 56 | 2.0595, 2.0677, 2.2479 |
| | red2a | 27 | 2.0743, 2.0777, 2.2730 |
| | red2r | 17 | 2.2886, 2.2339, 2.1797 |
| $MCR_{red1a}$ + HS−CoM + $CF_3$−S−CoB | red1cc | 68 | 2.0599, 2.0673, 2.2490 |
| | red2a | 24 | 2.0745, 2.0705, 2.2742 |
| | red2r | 8 | 2.2819, 2.2295, 2.1810 |

[a] Error in principle values: $\Delta g_i = 0.0005$.

is achieved with $CF_3$−S−CoB. In both [HS−CoB]-MCR and [$CF_3$−S−CoB]-MCR preparations the amount of $MCR_{red2}$ (and $MCR_{red1cc}$) induced is dependent upon the temperature of the sample before it is rapidly frozen, an effect reported in ref 28.

For each one of the EPR components $MCR_{red1cc}$, $MCR_{red2a}$, and $MCR_{red2r}$ the *g*-values listed in Table 1 are nearly the same regardless of whether HS−CoB, $CH_3$−S−CoB, or $CF_3$−S−CoB is bound. This indicates that coenzyme B and its two anaolgues induce very similar structural changes upon binding to the $MCR_{red1c}$ form.

In [HS−CoB]-MCR preparations, it is known that the induced $MCR_{red2r}$ species is distinguished by an Ni−S coordination,[39] a very large and anisotropic proton hyperfine

(39) Finazzo, C.; Harmer, J.; Bauer, C.; Jaun, B.; Duin, E. C.; Mahlert, F.; Goenrich, M.; Thauer, R. K.; Van Doorslaer, S.; Schweiger, A. *J. Am. Chem. Soc.* **2003**, *125* (17), 4988.

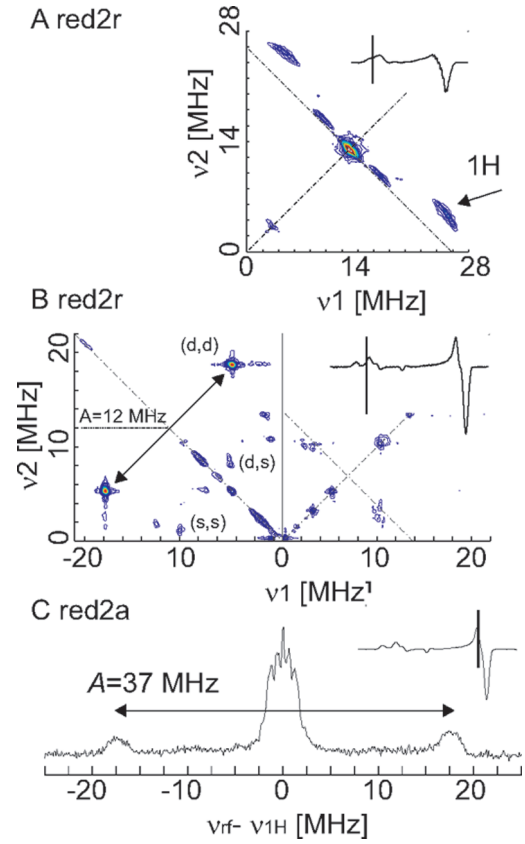


***Figure 2.*** (A) $^1$H X-band HYSCORE spectrum (9.723 GHz, 304.1 mT, $\tau$ = 120 ns). The marked cross-peaks shifted behind the $^1$H antidiagonal originate from a proton hyperfine coupling with a large anisotropy in $MCR_{red2r}$. (B) $^{14}$N Q-band HYSCORE spectrum (35.3515, 1120.9 mT, $\tau$ = 124 ns). The double- (d) and single-quantum (s) cross-peaks, which can be simulated with a nitrogen hyperfine coupling of ca. 12 MHz, belong to $MCR_{red2r}$. The double-quantum cross-peaks positions allow the hyperfine coupling to be evaluated as indicated. (C) Q-band Davies ENDOR spectrum (34.6767 GHz, 1193.0 mT) revealing a large proton hyperfine coupling of $|A(^1H)| = 37$ MHz from $MCR_{red2a}$. In A−C, the EPR spectrum and ENDOR/HYSCORE field position are shown in the inset.

interaction,[27] and an asymmetric spin density distribution on the four hydropyrrolic nitrogens.[29] The latter two features were confirmed for the new species [$CF_3$−S−CoB]-$MCR_{red2r}$. Figure 2A shows an X-band HYSCORE spectrum measured at the field position $g_1$ of $MCR_{red2r}$. Simulation of the set of $^1$H X-band HYSCORE (Figure S1, Supporting Information) and Q-band ENDOR (Figure S2, Supporting Information) spectra yielded the hyperfine couplings ($H_{rh}$) given in Table 2, which are very similar to those of the corresponding [HS−CoB]-$MCR_{red2r}$ preparation, $|A(^1H)| = [29, 26, 5]$ MHz. The small hydropyrrolic nitrogen hyperfine interaction previously found in $MCR_{red2r}$ induced with HS−CoB is also present with [$CF_3$−S−CoB] as is evident by the Q-band HYSCORE spectrum given in Figure 2B (Figure S3 displays the full set of data and simulations, Supporting Information). The hyperfine couplings given in Table 2 are very similar to those from the preparation [HS−CoB]-$MCR_{red2r}$ where $A(^{14}N) = [13.5, 16.0, 11.8]$ MHz. The remaining hydropyrrolic nitrogen hyperfine couplings are in the range $A(^{14}N) = 20-27$ MHz (data not shown). Measurement at the position of $g_{1,2}$ ($\equiv g_\perp$) of [$CF_3$−S−CoB]-$MCR_{red2a}$ (Figure 2C) reveals a very large and anisotropic proton ($H_{ax}$) hyperfine coupling that is very similar to $H_{ax}$ of [HS−CoB]-$MCR_{red2a}$, $A(^1H) = [-43,$

***Table 2.*** $^{1}$H, Pyrrole $^{14}$N, and $^{19}$F Hyperfine Couplings and Error Estimates (Δ) for the $MCR_{red2a}$, $MCR_{red2r}$, and $MCR_{red1cc}$ Species Induced with $CF_3$−S−CoB

| nucleus/comment | $A_1, A_2, A_3$ ($\Delta A_1, \Delta A_2, \Delta A_3$) [MHz] | α, β, γ[a] (Δα, Δβ, Δγ) | $a_{iso}$ [MHz] | $T_1, T_2, T_3$ [MHz] |
|---|---|---|---|---|
| | | $MCR_{red2a}$ | | |
| $^{1}H_{ax}$ (hydride) | −37.5, −34, −0.5 (1, 2, 1) | −, 0, 45 (−, 5, 5) | −23.6 | −13.8, −10.3, −24.2 |
| $^{14}N$ (×4)[g] | ∼22−38 | − | − | − |
| $^{19}F^{1}$[f] | −0.8, −0.8, 2.0 | 320, 11, 49 | 0.1 | −1.0, −0.9, 1.9 |
| $^{19}F^{2}$ | 1.7, 1.7, 3.9 | 85, 31, 287 | 2.4 | −0.7, −0.7, 1.4 |
| $^{19}F^{3}$ | −0.8, 0.4, 5.0 | 160, 38, 114 | 1.6 | −2.3, −1.2, 3.5 |
| | | $MCR_{red2r}$ | | |
| $^{1}H_{rh}$[d] | 28.0, 25.0, 4.0 [d] (1, 2, 1) | −130, 125, 60 (30, 10, 10) | 19.0[d] | 9.0, 6.0, −15.0[d] |
| $^{14}N$[b] | 11.5, 17.0, 11.5 | −, 30, 45 | 13.3 | −1.8, 3.6, −1.8 |
| $^{14}N$ (×3)[g] | ∼20−27 | − | − | − |
| $^{19}F^{1}$[e] | −0.1, −0.1, 2.4 | 260, 21, 89 | 0.7 | −0.9, −0.8, 1.7 |
| $^{19}F^{2}$ | 0.8, 0.8, 2.9 | 83, 15, 5 | 1.5 | −0.7, −0.7, 1.4 |
| $^{19}F^{3}$ | −1.5, −1.3, 3.1 | 170, 38, 100 | 0.1 | −1.6, −1.4, 3.0 |
| | | $MCR_{red1cc}$ | | |
| $^{14}N$ (×4)[g] | ∼27 | − | − | − |
| $^{19}F^{1}$ | −0.24, −0.24, 0.48 | −, 7, − | 0 | −0.24, −0.24, 0.48 |
| $^{19}F^{2}$ | −0.24, −0.24, 0.48 | −, 21, − | 0 | −0.27, −0.27, 0.56 |
| $^{19}F^{3}$ | −0.49, −0.49, 0.96 | −, 15, − | 0 | −0.49, −0.49, 0.96 |

[a] Euler angles define the passive rotation of the hyperfine or nuclear quadrupole principal axis system into the *g*-matrix principal axis system, $A = \mathbf{R}(\alpha,\beta,\gamma)A_{diagonal}\mathbf{R}^{\dagger}(\alpha,\beta,\gamma)$. [b] Nuclear quadrupole parameters $|e^2qQ/h| = 3.25$ MHz, $\eta = 0.6$, and $[\alpha,\beta,\gamma] = [0,-60,135]$, where $\kappa = |e^2qQ/h|/4I(2I-1)$) and asymmetry parameters $\eta = (Q_1 - Q_2)/Q_3$ with $Q_1 = -\kappa(1-\eta)$, $Q_2 = -\kappa(1+\eta)$, and $Q_3 = 2\kappa$. [c] Several values of $\gamma$ (α) give similar simulations; no error estimate is given. [d] Absolute sign of interaction unknown. [e] Values for the $\rho(S) = 0.17$. [f] Values for the $\rho(S) = 0.04$. [g] Range of pyrrole nitrogen hyperfine coupling from refs 23, 29, and 38.

−42, −5] MHz (Figures S1−S2 display the data set, Supporting Information).

The *g*-values and hyperfine couplings show conclusively that the nature of the three EPR components induced by addition of either the natural substrate H−S−CoB or the analog $CF_3$−S−CoB results in nickel-centered paramagnetic species with very similar structures and CoB bindings.

We now turn our attention to locating the $CF_3$ position (of $CF_3$−S−CoB) for the three species. Fluorine signals from the [$CF_3$−S−CoB] preparation are observed with W-band Mims ENDOR as shown in Figure 3; spectra c−j have contributions from $MCR_{red1cc}$, b−i from $MCR_{red2a}$, and $MCR_{red2r}$ contributes to traces a−e. The three fluorine $C^{19}F_3$−S−CoB hyperfine couplings for each species (red1cc/red2a/red2r) were modeled with an isotropic $a_{iso}$ and a dipole contribution with principal values [$T_1$, $T_2$, $T_3$] MHz, the latter calculated according to the point-dipole model, [40]

$$\mathbf{T} = \sum_k \mathbf{R}_k(\alpha,\beta,\gamma)T_k diag(-1,-1,2)\mathbf{R}_k^{\dagger}(\alpha,\beta,\gamma) \tag{2A}$$

with

$$T_k = (\mu_o/4\pi h)(g_e\beta_e g_n\beta_n)\rho_k\frac{1}{r_k^3} \tag{2B}$$

where $r_k$ is the distance between the unpaired electron and the $k^{th}$ nucleus with spin population $\rho_k$, and $\mathbf{R}(\alpha,\beta,\gamma)$ is the rotation matrix transforming the $k^{th}$ point-dipole contribution into the *g*-matrix principal axis system. In calculations using eq 2A, the following spin populations were assumed unless stated otherwise; $MCR_{red1cc}$ $\rho(Ni) = 88\%$, each hydropyrrolic nitrogen $\rho(N) = 3\%$; $MCR_{red2a}$ $\rho(Ni) = 84\%$, thiol $\rho(S) \le 4\%$; each hydropyrrolic nitrogen $\rho(N) = 3\%$; $MCR_{red2r}$ $\rho(Ni) = 71-82\%$, thiol $\rho(S) = 17-6\%$,[41] three hydropyrrolic nitrogen as $\rho(N) = 3\%$ and the fourth as $\rho(N) = 1.5\%$.

For each species, ENDOR spectra are simulated with three $^{19}$F hyperfine couplings,

$$\mathbf{A}^i = a_{iso}^i + \mathbf{T}^i(R)\ (i = 1,2,3) \tag{3}$$

and fitted to the experimental traces by optimizing the three $a_{iso}^i$ values and the positions of $CF_3$−(S−CoB) relative to $NiF_{430}$ by changing **R** and $r_k$ in eqs 2A/B. This equates to moving $CF_3$ in the **x**, **y**, or **z** directions and rotation of $CF_3$ around the S−C bond, $d\mathbf{T}_k = d\mathbf{T}_k(dx,dy,dz,d\theta)$. Optimized $^{19}$F couplings and the corresponding fits are shown in Table 2 and Figure 3, respectively.

The ENDOR spectrum recorded at the highest field position, Figure 3j, is contributed to by only $MCR_{red1cc}$ and has a hyperfine coupling at $g_{1,2}$ (≡ $g_\perp$) of $|A_{1,2}| \approx 0.4$ MHz. This coupling can be accounted for when [$CF_3$−S−CoB] is positioned as in the $Ni^{II}$ crystal structure (i.e., simply by replacing the thiol H with $CF_3$, see Scheme 2A) giving the three Ni−F distances between $r = 6.3-7.6$ Å. The point-dipolar model of Eq. 2A then gives $A_{1,2}^{calc} = -(0.21-0.46)$ MHz and $A_3^{calc} = +(0.43-0.91)$ MHz[42] (see Table 2) since the $g_3$-axis ($g_{||}$-axis) is known to point perpendicular to the $NiF_{430}$ plane. The fluorine signals for $MCR_{red1cc}$ are thus accurately modeled by only dipolar contributions ($a_{iso}^i = 0$) with [$CF_3$−S−CoB] positioned according the crystal structure of $Ni^{II}$ MCR (Scheme 2A).

To simulate the $MCR_{red2a}$ signals at field positions b-i the hyperfine model needed both isotropic and dipolar contributions as listed in Table 2. This is a significant result as it indicates an electronic connection between the nickel ion and the F nuclei,

(40) Pöppl, A.; Kevan, L. *J. Phys. Chem.* **1996**, *100* (9), 3387.

(41) Spin population is based on the $^{33}$S hyperfine interaction, for which the sign of the principal values could not be determined. This results in the two value of 6 or 17%.

(42) The hyperfine coupling between an electron localised at a point and a nuclear spin is (−*T*,−*T*,2*T*), where the largest value has its axis along the electron−nuclear vector.

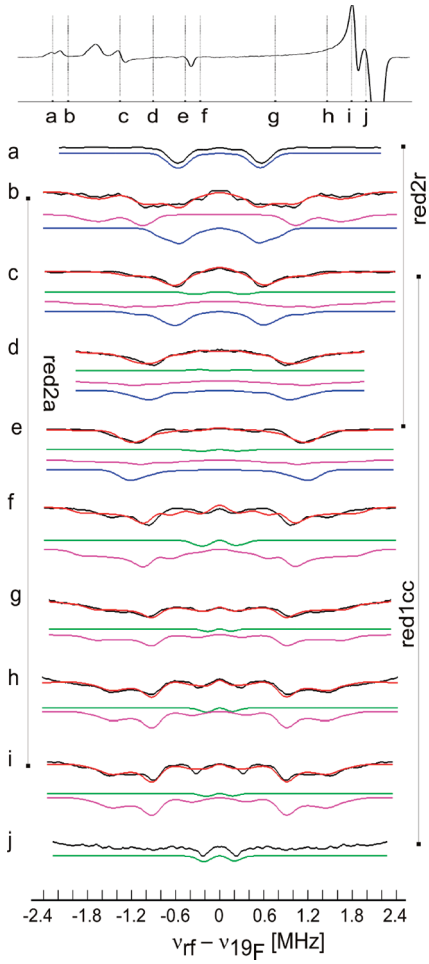


***Figure 3.*** W-band (94.255 GHz) Mims ENDOR spectra recorded at 15 K showing the $^{19}F$ frequency region. Experimental, black. Simulations: total, red; red1cc, green (b−j); red2a, magenta (b−i); and red2r, blue (a−e). The $B_0$ observer positions (mT) and $\tau$ values (ns) are (A) 2954, $\tau$ = 200, 400, (B) 2969, $\tau$ = 200, (C) 3019, $\tau$ = 200, 500, (D) 3051, $\tau$ = 200, 500, (E) 3082, $\tau$ = 200, 400, (F) 3096, $\tau$ = 200, 400, (G) 3169, $\tau$ = 200, 600, (H) 3219, $\tau$ = 200, 500, (I) 3242, $\tau$ = 200, and (J) 3251, $\tau$ = 200, 400.

probably mediated through the coordinated Ni−H−S−CoM moiety (see Scheme 2B). Clearly the hyperfine couplings are much larger than those from $MCR_{red1cc}$ as can be appreciated by comparing trace j (only $MCR_{red1cc}$) to i ($g_{1,2}$ of $MCR_{red2a}$/$MCR_{red1cc}$) which shows a hyperfine coupling of $|A_{1,2}(^{19}F)|^{max}$ = 4 MHz belonging to $MCR_{red2a}$. The magnitude of this very important coupling was confirmed by X-band HYEND (Figure S4, Supporting Information) and Q-band Mims ENDOR measurements (Figure S5, Supporting Information) and cannot be purely dipolar for several reasons. First, this would imply $A(^{19}F)^{max} \approx [-4,-4,8]$ MHz since the $\boldsymbol{g}_3$ axis and $\boldsymbol{A}_3$ axis are perpendicular to the $F_{430}$ macrocycle and $CF_3$−S−CoB is located near the $\boldsymbol{g}_3$ axis. This would give $r$(Ni−F) = 2.7 Å for $\rho$(Ni) = 1, improbably short since, in $MCR_{red2a}$, the "hydride" hydrogen is located axially at ca. 1.7 Å above the nickel, and H−S−CoM is known to be close to the nickel as well (via hyperfine couplings of the $\beta$-protons).[27] Second, the field dependence of the $^{19}F$ signal is not dramatic and at all ENDOR observer field positions $A(^{19}F)^{max}$ < 4.5 MHz. Third, such a large anisotropy would easily be detected with X-band HYSCORE measurements, which is not the case (data not shown). For an isotropic hyperfine contribution $a_{iso}$ the fluorine orbital must overlap with a thiol(ate) S orbital from CoM, implying a shortening of the

***Scheme 2.*** Schematic Representation of the $CF_3$−S−CoB Positions as Determined by $^{19}F$ ENDOR Measurements[a]

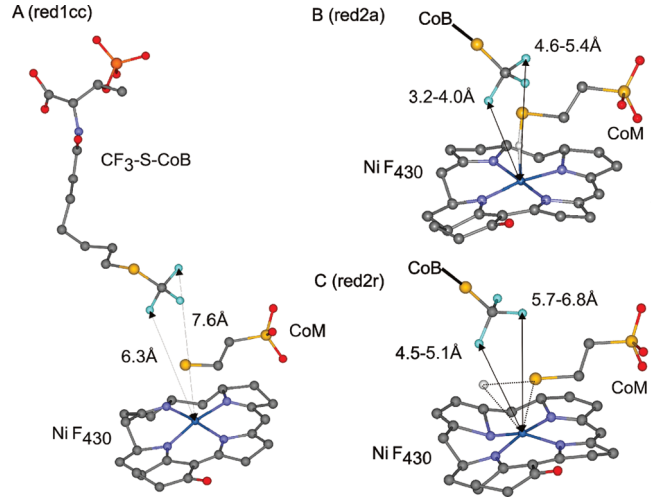


[a] (A) $MCR_{red1cc}$ with distances $r$(Ni−F) = 6.3, 7.5, 7.6 Å, which are essentially those expected assuming the crystal structure of inactive Ni(II) enzyme. (B) A DFT model of $MCR_{red2a}$ with H−S−CoM coordinated, $r$(Ni−S) = 3.1 Å and $r$(Ni−H) = 1.7 Å.[27] Arrows indicate the shortest and longest Ni−F distances for sulfur spin densities of 0 and 0.04 (for $\rho$(S) = 0.04; $r$(Ni−F) = 4.0, 5.0, 5.4 Å and $r$(S−F) = 1.5, 2.1, 2.5 Å). (C) $MCR_{red2r}$ where EPR has established a strong Ni−S coordination, a strongly coupled proton, and asymmetric pyrrole nitrogen hyperfine couplings; the structure is a hypothesis consistent with this data.[27] The Ni−F distances indicated by the arrows are for $\rho$(S) = 0.06 and 0.17, and $r$(Ni−S) = 2.5 Å (for $\rho$(S) = 0.17; $r$(Ni−F) = 5.1, 5.9, 6.8 Å and $r$(F−S) = 2.1, 2.9, 3.9 Å).

Ni−F distances. The optimized parameters for $MCR_{red2a}$, obtained from simulations using $\rho$(S) = 0.04, are listed in Table 2. The dipolar parts of the three hyperfine couplings indicate a shorting of the Ni−F distances from 6.2−7.7 Å to 4.0−5.5 Å (Scheme 2B), consistent with direct contact between fluorine atoms and the sulfur of CoM. The result is sensitive to the spin density distribution on the S of CoM, and $\rho$(S) = 0.04 is an upper limit and thus the distances are also upper limits. Using $\rho$(S) = 0 reduces the Ni−F distances to 3.2−4.6 Å.

Simulations for $MCR_{red2r}$ are determined from the five spectra of Figure 3a−e. The spectrum at the lowest field position (a) showing $|A_1(^{19}F)|$ = 0.9−1.5 MHz is contributed to only by the $MCR_{red2r}$ species and only those molecular orientations close to its $g_1$ axis. In this species the spin density on the coordinated thiol(ate) sulfur is estimated from $^{33}S$ EPR data in the range $\rho$(S) = 0.06−0.17.[39] Taking the upper limit of $\rho$(S) = 0.17, the maximum fluorine dipolar coupling according to Eq. 2A with $CF_3$−S−CoB positioned according the X-ray structure of the inactive Ni(II) enzyme would be $A_{||}^{cal}$ = 1.2 MHz. This value occurs directly along the electron−nuclear vector, which is expected to be close to the $\boldsymbol{g}_3$ axis that points closely along the Ni−S bond.[39] The calculated two perpendicular values would be $A_{\perp}^{cal}$ = −0.6 MHz. Thus even in the impossible case where the $g_1$ axis points near to the Ni−F and S−F vectors, the calculated coupling is too small to account for the experimental one, indicating the $CF_3$−S−CoB nickel distance has shortened, and probably that there is also an isotropic contribution. The final optimized hyperfine parameters are given in Table 2, and as for $MCR_{red2a}$, the presence of the isotropic $^{19}F$ couplings indicates an orbital overlap with the thiol sulfur of (H)S−CoM and a reduction in the Ni−F distances to $r$(Ni−F) = 5.1−6.8 Å. Simulation using the lowest thiol(ate) spin density, $\rho$(S) =

0.06, yields considerably shorter Ni−F distances of $r$(Ni−F) = 4.5−5.7 Å.

## Conclusion

The Ni−$^{19}$F hyperfine couplings presented above leave no doubt that in $MCR_{red2a}$ and $MCR_{red2r}$, the two species induced upon binding of $CF_3$−S−CoB to $MCR_{red1c}$, the distance between the trifluoromethyl group and the nickel center is distinctly reduced as compared to $MCR_{red1cc}$ (with couplings that are described very well assuming $CF_3$−S−CoB positioned as in the $Ni^{II}F_{430}$ X-ray structure).

Since the EPR and ENDOR spectra of the $MCR_{red2}$ forms induced by binding of coenzyme B or its analogs *S*-methyl coenzyme B and *S*-trifluoromethyl coenzyme B are very similar and show the same three EPR species, it is reasonable to assume that all three are bound to the enzyme in the same way and induce the same structural changes in the protein and the coordination environment of the nickel in $F_{430}$. The enzyme is not inactivated by the fluorine labeled inhibitor: $CF_3$−S−CoB in the presence of coenzyme M does not quench the $MCR_{red1}$ signal and reversibly converts $MCR_{red1}$ to $MCR_{red2}$ signals to the same extent as $CH_3$−S−CoB. The latter has been shown to reversibly inhibit MCR, inhibition being competitive with respect to HS−CoB and noncompetitive with respect to $CH_3$−S−CoM.[30,43]

Inspection of the X-ray crystal structure of the inactive Ni(II) form $MCR_{ox1\text{-}silent}$, which also has one molecule of coenzyme B and one molecule of coenzyme M bound in the active site, reveals that the polar groups of the threonine posphate end of coenzyme B are fixed by numerous hydrogen bonds to the amino acids lining the funnel-shaped entrance near the enzyme surface whereas the 7-thioheptanoyl chain tightly fits into a long narrow channel formed by hydrophobic amino acid side chains, which connects the entrance funnel to the dome-shaped cavity above the proximal face of the nickel hydrocorphin macrocycle (Figure 4). The 7-thioheptanoyl chain assumes a $t,t,g^+,g^+,g^+,t$ conformation with a bend that follows a corresponding kink of ca. 120° in the protein channel. The terminal thiol group is located at the exit of the channel into the cavity in which coenzyme M is bound.

An additional trifluoromethyl group bound to the sulfur of coenzyme B can be modeled into the rigid structure of $MCR_{ox1\text{-}silent}$ without steric clashes; it protrudes into the proximal pocket directly above the thiol group of bound coenzyme M. In this model, in which the protein structure remains the same as in $MCR_{ox1\text{-}silent}$, the shortest distance between a fluorine atom and nickel is 6.25 Å. This distance corresponds closely to the value deduced from the hyperfine data for the $MCR_{red1cc}$ component of our $MCR_{red2a/r}$−$MCR_{red1cc}$ sample, namely 6.3 Å.

In contrast to $MCR_{red1cc}$, the closest distances between $^{19}$F and Ni deduced for the $MCR_{red2a}$ and the $MCR_{red2r}$ species of 3.2−4.0 Å and 4.5−5.1 Å, respectively, are much shorter than anticipated based on the $MCR_{ox1\text{-}silent}$ crystal structure. The possibility that the trifluoromethyl group is transferred from the sulfur of coenzyme B to the one of coenzyme M inside the enzyme can be excluded because we have shown earlier that $CF_3$−S−CoM in the presence of coenzyme B quenches the Ni(I) signal to give an organic radical.[44] Within the rigid framework of the $MCR_{ox1\text{-}silent}$ structure, the possibility that coenzyme B could slide down the channel into a second binding site can be excluded because this would lead to a loss of the hydrogen bonds of the threonine phosphate moiety with polar protein residues, and the channel is too narrow to accommodate this part of coenzyme B (Figure 4). Attempts to model a more extended $t,t,t,t,t,t$ conformation of coenzyme B, which might be able to reach to within the measured distances, into the $MCR_{ox1\text{-}silent}$ structure failed because they lead to prohibitive van der Waals clashes with the protein in the region of the bend in the channel. We therefore conclude that, upon the transformation of $MCR_{red1c}$ into $MCR_{red2a}$ and $MCR_{red2r}$, induced by binding of coenzyme B and its analogs, the protein must undergo a significant conformational change.

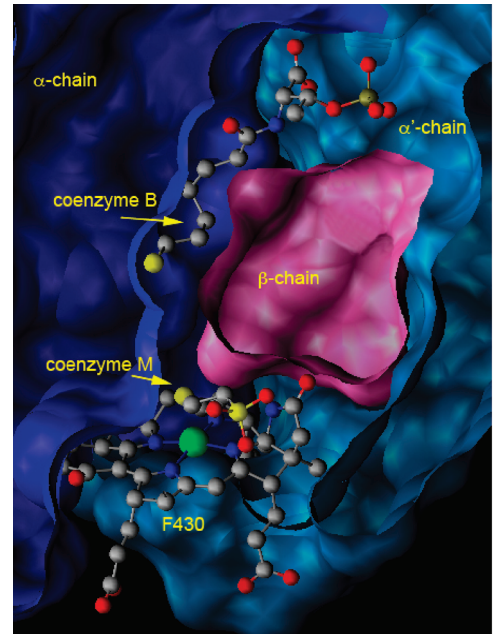


***Figure 4.*** Active site of MCR-I in the inactive Ni(II) form $MCR_{ox1\text{-}silent}$ with bound coenzymes B and M. Shown is a cut through the surfaces of the protein at the interfaces of the α-, α′- and β-chains, which form the polar entrance funnel, the long, narrow, hydrophobic channel with its bend, and the dome-shaped cavity above the Ni-hydrocorphinoid $F_{430}$. PDB code: 1MRO.[3]

It has been shown earlier that the binding of coenzyme B converts at most 50% of the spins of $MCR_{red1c}$ into $MCR_{red2a}$ plus $MCR_{red2r}$ and that the two $MCR_{red2}$ species are in a temperature dependent equilibrium.[28] The fact that at least 50% of the $MCR_{red1cc}$ signal remains after addition of coenzyme B has been discussed in the terms of a hypothetical two-stroke mechanism in which the two symmetry related active sites of the enzyme are coupled and not synchronously in the same state during catalysis. The weak but significant hyperfine coupling between the $^{19}$F atoms of $CF_3$−S−CoB and the unpaired electron on the nickel center of the $MCR_{red1cc}$ component reported here proves that the coenzyme B analog is also bound to active sites that are not converted into $MCR_{red2r}$ or $MCR_{red2a}$. Since binding of coenzyme B or its analogs is triggering the formation of the $MCR_{red2}$ species, the question arises why active sites remain in the $MCR_{red1cc}$ state despite the fact that they have coenzyme B bound. This question has to remain open because ENDOR experiments do not directly measure pair−pair relationships and cannot correlate the presence of $MCR_{red1cc}$ and $MCR_{red2}$ forms in the *same* enzyme molecule. However, one possible explanation would be that the conformational change in the protein induced upon transformation to $MCR_{red2r}$ or

(43) Goenrich, M.; Duin, E. C.; Mahlert, F.; Thauer, R. K. *J. Biol. Inorg. Chem.* **2005**, *10*, 333.
(44) Goenrich, M.; Mahlert, F.; Duin, E. C.; Bauer, C.; Jaun, B.; Thauer, R. K. *J. Biol. Inorg. Chem.* **2004**, *9*, 691.

$MCR_{red2a}$ prevents the formation of these species in the other active site. Although the X-ray structures do not directly provide support for an asymmetric "2-stroke" catalytic cycle, they interestingly reveal that both active sites are interlinked via the two α subunits, both of which contribute to the formation of both active sites.

None of the species investigated here ($MCR_{red1cc}$, $MCR_{red2a}$, $MCR_{red2r}$) is a logical candidate for an intermediate in the catalytic cycle of methane formation because, instead of the natural substrate methyl coenzyme M, they contain the competitive substrate analog coenzyme M. So far, no intermediate of the catalytic cycle with the natural substrates has been observed, the only state detected by EPR during catalysis being the $MCR_{red1m}$ state with the first substrate, methyl coenzyme M, bound and the second substrate, coenzyme B, absent.[45] However, the detection of a significant conformational change of the protein concomitant with the formation of the $MCR_{red2}$ species reported here is relevant to the mechanistic question. The X-ray structure of the inactive Ni(II) forms of MCR, which are very compact and tightly packed around the active site, certainly biased thinking about possible mechanisms because it is difficult to envisage a change in the coordination geometry and conformation of the tetrapyrrolic cofactor without a major conformational change involving several protein chains. To our knowledge, the mechanisms proposed so far only postulate catalytic intermediates in which the coordination geometry of the nickel center was either square planar, square pyramidal, or elongated octahedral. We have shown previously[27,39] that in $MCR_{red2r}$ at least one of the tetrapyrrolic nitrogens of $F_{430}$ has a much reduced hyperfine coupling compared to the others and that the nickel is bound to both, the sulfur of coenzyme M and a hydrogen at <2.25 Å. This lead us to suggest a coordination geometry with two substrate derived cis-ligands on the same face of the macrocycle and one of the nitrogens of $F_{430}$ moved into an off-equatorial position. The finding that the protein does undergo a significant conformational change upon formation of the $MCR_{red2}$ species helps to rationalize these earlier data because any movement of one of the tetrapyrrolic nitrogens away from the equatorial plane requires a conformational change in the protein chains tightly anchoring the sidechains of $F_{430}$ in the $MCR_{ox1\text{-}silent}$ structure. Together, these studies open up the possibility that coordination geometries other than square planar, square pyramidal or elongated octahedral are accessible. The mechanisms proposed for nonenzymatic C−H activation reactions at transition metal centers typically require intermediates in which two fragments of the reacting hydrocarbon occupy two cis-coordination sites on the metal.[46−48] Furthermore, there is increasing evidence that anaerobic methane oxidation by archaea of the ANME type, that is, activation of a C−H bond in methane, is catalyzed by enzymes that are close homologues of MCR and contain either coenzyme $F_{430}$ or the variant $17^2$-methylthio-coenzyme $F_{430}$.[49,50] In view of these observations, the possibility that methyl-coenzyme M reductase can adjust its conformation to allow coordination geometries with two cis-ligands on the proximal face of $F_{430}$ is of particular interest.

**Acknowledgment.** We thank the ETH Zürich, the Swiss National Science Foundation (SNF), the Max Planck Society, and the EPSRC and BBSRC for financial support.

**Supporting Information Available:** Figures S1−S5. This material is available free of charge via the Internet at http://pubs.acs.org.

JA906367H

(45) Krzycki and Prince have observed formation of the $MCR_{red2r}$ signal in whole cells of Methanosarcina barkeri after cessation of linear methane formation from acetate: Krzycki, J. A.; Prince, R. C. *Biochim. Biophys. Acta* **1990**, *1015*, 53.

(46) Janowicz, A. H.; Bergman, R. G. *J. Am. Chem. Soc.* **1982**, *104*, 352.
(47) Perutz, R. N.; Sabo-Etienne, S. *Angew. Chem., Int. Ed.* **2007**, *46*, 2578.
(48) Crabtree, R. H. *J. Organomet. Chem.* **2004**, *689*, 4083.
(49) Krueger, M.; Meyerdierks, A.; Gloeckner, F. O.; Amann, R.; Widdel, F.; Kube, M.; Reinhardt, R.; Kahnt, J.; Boecher, R.; Thauer, R. K.; Shima, S. *Nature* **2003**, *426* (6968), 878.
(50) Mayr, S.; Latkoczy, C.; Kruger, M.; Gunther, D.; Shima, S.; Thauer, R. K.; Widdel, F.; Jaun, B. *J. Am. Chem. Soc.* **2008**, *130* (32), 10758.